

## Non-Matching Grids for a Flexible Discretization in Computational Acoustics

Bernd Flemisch<sup>1</sup>, Manfred Kaltenbacher<sup>2,\*</sup>, Simon Triebenbacher<sup>2</sup>  
and Barbara Wohlmuth<sup>3</sup>

<sup>1</sup> *Institute of Hydraulic Engineering, University of Stuttgart, Germany.*

<sup>2</sup> *Applied Mechatronics, Alps-Adriatic University Klagenfurt, Austria.*

<sup>3</sup> *Department of Numerical Mathematics, Technical University of Munich, Germany.*

Received 14 December 2009; Accepted (in revised version) 28 August 2010

Available online 24 October 2011

---

**Abstract.** Flexible discretization techniques for the approximative solution of coupled wave propagation problems are investigated. In particular, the advantages of using non-matching grids are presented, when one subregion has to be resolved by a substantially finer grid than the other subregion. We present the non-matching grid technique for the case of a mechanical-acoustic coupled as well as for acoustic-acoustic coupled systems. For the first case, the problem formulation remains essentially the same as for the matching situation, while for the acoustic-acoustic coupling, the formulation is enhanced with Lagrange multipliers within the framework of Mortar Finite Element Methods. The applications will clearly demonstrate the superiority of the Mortar Finite Element Method over the standard Finite Element Method both concerning the flexibility for the mesh generation as well as the computational time.

**AMS subject classifications:** 65L60, 74S05

**Key words:** Nonmatching grids, Mortar FEM, computational acoustics, piezoelectric actuators.

---

## 1 Introduction

In many engineering applications vibrations are responsible for the generation of acoustic noise. Especially slender or thin-walled structures with a large surface exhibit such a behavior. A modern way of controlling those vibrations is to attach piezoelectric patches to membrane/plate like structures which can measure their deformations and by using adequate power electronics act against the vibrations. These enhanced devices are so-called smart materials.

---

\*Corresponding author. *Email addresses:* Bernd.Flemisch@iws.uni-stuttgart.de (B. Flemisch), manfred.kaltenbacher@aau.at (M. Kaltenbacher), simon.triebenbacher@aau.at (S. Triebenbacher), barbara.wohlmuth@ma.tum.de (B. Wohlmuth)

It is our goal to simulate such devices by applying the Finite Element Method (FEM). The standard method does not offer enough flexibility to freely place the piezoelectric actuators on the membrane/plate structures. We therefore resort to use the Mortar FEM. In both structures we solve for the partial differential equation (PDE) describing the effects of linear elasticity. In the piezoelectric actuator the electric-mechanical coupling has to be taken into account additionally. The continuity of the normal stresses between the membrane/plate structure and the piezoelectric actuator is maintained by introducing a Lagrange multiplier. Now, the discretizations of both parts need not match on the common surfaces any more and we are therefore allowed to freely place the piezoelectric actuators on the membranes/plates. Therefore, we have to deal with the situation of nonconforming grids appearing at the common interface of two subdomains. Special care has to be taken in order to define and implement the appropriate discrete coupling operators (see, e.g., [2, 4, 6, 11, 17]).

In this contribution we extend our research first published in [9] to full multiphysics application including nonmatching mechanical-mechanical and mechanical-acoustic interfaces. Therewith, we apply the method to practically relevant application, e.g., piezoelectric patches attached to mechanical structures for active vibration as well as noise control. In order to simulate the noise radiated from a vibrating structure we once again apply nonmatching grids and extend the computational mesh for the plate by a mesh for acoustic propagation. In this case however, no Lagrange multiplier is required since the coupling takes place between two different physical quantities (mechanical displacement and acoustic pressure).

The rest of this paper is organized in the following way. In Section 2 we introduce the basic equations of linear piezoelectricity, the coupling scheme for mechanics on nonmatching grids, and the coupling between the mechanical field with the acoustic field. In Section 3 we describe the application of our enhanced scheme for the numerical computation of a metal plate with attached piezoelectric patches. A summary and conclusions are given at the end.

## 2 Governing equations and numerical scheme

### 2.1 Equations of linear piezoelectricity

The linearized material law describing the piezoelectric effect is given by [13]

$$\boldsymbol{\sigma} = [c^E] \mathbf{S} - [e]^t \mathbf{E}, \quad (2.1)$$

$$\mathbf{D} = [e] \mathbf{S} + [\varepsilon^S] \mathbf{E}. \quad (2.2)$$

Here  $\boldsymbol{\sigma}$  is the tensor of mechanical stresses in Voigt notation,  $[c^E]$  the linear stiffness tensor at constant electric field,  $\mathbf{S}$  denotes the tensor of mechanical strains (also in Voigt notation),  $[e]$  the tensor of piezoelectric coupling coefficients ( $\square^t$  denotes the transposed),  $\mathbf{E}$  the electric field vector,  $\mathbf{D}$  the vector of the electric flux density and finally  $[\varepsilon^S]$  the tensor

of electric permittivity coefficients at constant strain. To describe the linear mechanical behavior of a piezoelectric system we start at Navier's equation

$$f_{\Omega} + \mathcal{B}^t \sigma = \rho a, \quad (2.3)$$

where  $f_{\Omega}$  denotes a volume force acting on the structure,  $\mathcal{B}^t$  is the divergence operator applied to the tensor of mechanical stresses  $\sigma$  in Voigt notation (potential energy) and the right hand side describes the inertia force acting on a body (kinetic energy). By using the strain-displacement relation  $\mathbf{S} = \mathcal{B}\mathbf{u}$  and (2.1), we can rewrite (2.3) in the following form

$$\rho \ddot{\mathbf{u}} - \mathcal{B}^t([\mathbf{c}^E]\mathcal{B}\mathbf{u} - [\mathbf{e}]^t \mathbf{E}) = f_{\Omega}. \quad (2.4)$$

Due to the fact, that piezoelectric materials are insulators, the divergence of the electric flux has to be equal to zero

$$\nabla \cdot \mathbf{D} = 0. \quad (2.5)$$

Since we assume no time varying magnetic field, the *curl* of the electric field intensity  $\mathbf{E}$  is zero (second Maxwell's equation [13]) and we may express it by the scalar electric potential  $V$  via

$$\mathbf{E} = -\nabla V. \quad (2.6)$$

Therewith, one may rewrite Eq. (2.4)

$$\rho \ddot{\mathbf{u}} - \mathcal{B}^t([\mathbf{c}^E]\mathcal{B}\mathbf{u} + [\mathbf{e}]^t \nabla V) = f_{\Omega}, \quad (2.7)$$

and also Eq. (2.5) may be rewritten by additionally using Eq. (2.2) for  $\mathbf{D}$

$$\nabla \cdot ([\mathbf{e}]\mathcal{B}\mathbf{u} - [\varepsilon^S]\nabla V) = 0. \quad (2.8)$$

For the finite element formulation of the piezoelectric problem setting, we define the computational domain as in Fig. 1. We fix the mechanical displacement  $\mathbf{u}$  and the electric potential  $V$  on the grounded electrode by applying homogeneous Dirichlet boundary conditions. On the loaded electrode we fix the electric potential to  $V_e$  and leave the mechanical displacement free by applying a homogeneous Neumann boundary condition. On the other two boundaries homogeneous Neumann boundary conditions for the scalar electric potential as well as the mechanical displacement are used. The strong formulation of the setting above is as follows: Given the initial fields and material parameters

$$\begin{aligned} \mathbf{u}_0 &: \Omega \rightarrow \mathbb{R}^d, \\ \dot{\mathbf{u}}_0 &: \Omega \rightarrow \mathbb{R}^d, \\ V_0 &: \Omega \rightarrow \mathbb{R}, \\ \rho, c_{ij}, e_{ij}, \varepsilon_{ij} &: \Omega \rightarrow \mathbb{R}. \end{aligned}$$

Find

$$\begin{aligned} \mathbf{u}(t) &: \overline{\Omega} \times [0, T] \rightarrow \mathbb{R}^d, \\ V(t) &: \overline{\Omega} \times [0, T] \rightarrow \mathbb{R}, \end{aligned}$$

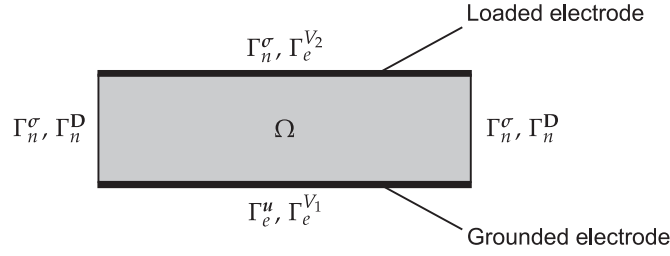


Figure 1: Setup for piezoelectric FE formulation.

such that

$$\rho \ddot{\mathbf{u}} - \mathcal{B}^t([\mathbf{c}^E] \mathcal{B} \mathbf{u} - [\mathbf{e}]^t \nabla V) = 0, \quad (2.9)$$

$$\nabla \cdot ([\mathbf{e}] \mathcal{B} \mathbf{u} + [\boldsymbol{\varepsilon}^S] \nabla V) = 0, \quad (2.10)$$

together with the boundary conditions

$$\begin{aligned} \mathbf{u} &= 0, & \text{on } \Gamma_e^u \times (0, T), \\ V &= 0, & \text{on } \Gamma_e^{V1} \times (0, T), \\ V &= V_e, & \text{on } \Gamma_e^{V2} \times (0, T), \\ \mathbf{n} \cdot [\boldsymbol{\sigma}] &= 0, & \text{on } \Gamma_n^\sigma \times (0, T), \\ \mathbf{n} \cdot \mathbf{D} &= 0, & \text{on } \Gamma_n^D \times (0, T), \end{aligned}$$

and initial conditions

$$\begin{aligned} \mathbf{u}(\mathbf{r}, 0) &= \mathbf{u}_0, & \mathbf{r} \in \Omega, \\ \dot{\mathbf{u}}(\mathbf{r}, 0) &= \dot{\mathbf{u}}_0, & \mathbf{r} \in \Omega \end{aligned}$$

are satisfied. We then derive the weak formulation of the problem by multiplying (2.9) and (2.10) by appropriate test functions  $\mathbf{u}'$ ,  $\psi$  and applying Green's integral theorem. Therewith, we arrive at the weak (variational) formulation: Find  $(\mathbf{u}, V) \in \mathcal{V}_0 \times \mathcal{W}_{V_e}$  such that<sup>†</sup>

$$\int_{\Omega} \rho \mathbf{u}' \cdot \ddot{\mathbf{u}} \, d\Omega + \int_{\Omega} (\mathcal{B} \mathbf{u}')^t [\mathbf{c}^E] \mathcal{B} \mathbf{u} \, d\Omega + \int_{\Omega} (\mathcal{B} \mathbf{u}')^t [\mathbf{e}]^t \tilde{\mathcal{B}} V \, d\Omega = 0, \quad (2.11a)$$

$$\int_{\Omega} (\tilde{\mathcal{B}} \psi)^t [\mathbf{e}] (\mathcal{B} \mathbf{u}) \, d\Omega - \int_{\Omega} (\tilde{\mathcal{B}} \psi)^t [\boldsymbol{\varepsilon}^S] \tilde{\mathcal{B}} V \, d\Omega = 0 \quad (2.11b)$$

is fulfilled for all  $(\mathbf{u}', \psi) \in \mathcal{V}_0 \times \mathcal{W}_0$ . In (2.11)  $\tilde{\mathcal{B}} = (\partial/\partial x, \partial/\partial y, \partial/\partial z)^t$  is the gradient of a scalar function and  $n_d$  the space dimension. We spatially discretize using standard finite

<sup>†</sup>With  $\mathcal{V}_0 = \{ \mathbf{v} \in (H^1)^{n_d} \mid \mathbf{v} = 0 \text{ on } \Gamma_e^u \}$ ,  $\mathcal{W} = \{ q \in H^1 \mid q = 0 \text{ on } \Gamma_e^{V1}, q = V_e \text{ on } \Gamma_e^{V2} \}$  and  $H^1$  denotes the Sobolev space as defined in [1].

elements with Lagrange basis functions and denote by  $n_n$  the number of nodes with unknown displacement and electric potential in the mesh

$$\mathbf{u} \approx \mathbf{u}^h = \sum_{i=1}^{n_d} \sum_{a=1}^{n_n} N_a u_{ia} \mathbf{e}_i = \sum_{a=1}^{n_n} \mathbf{N}_a \mathbf{u}_a, \quad \mathbf{N}_a = \begin{pmatrix} N_a & 0 & 0 \\ 0 & N_a & 0 \\ 0 & 0 & N_a \end{pmatrix},$$

$$V \approx V^h = \sum_{a=1}^{n_n} N_a V_a.$$

We therefore obtain the semi-discrete system of equations

$$\begin{pmatrix} \mathbf{M}_u & 0 \\ 0 & 0 \end{pmatrix} \begin{pmatrix} \ddot{\mathbf{u}} \\ \ddot{\underline{V}} \end{pmatrix} + \begin{pmatrix} \mathbf{C}_u & 0 \\ 0 & 0 \end{pmatrix} \begin{pmatrix} \dot{\mathbf{u}} \\ \dot{\underline{V}} \end{pmatrix} + \begin{pmatrix} \mathbf{K}_u & \mathbf{K}_{uV} \\ \mathbf{K}_{uV}^t & -\mathbf{K}_{VV} \end{pmatrix} \begin{pmatrix} \mathbf{u} \\ \underline{V} \end{pmatrix} = \begin{pmatrix} 0 \\ \underline{f}_e \end{pmatrix}$$

with an additional mechanical damping matrix  $\mathbf{C}_u$ , which models a velocity proportional damping. We apply the Rayleigh damping model for which the damping matrix computes as  $\mathbf{C}_u = \alpha \mathbf{M}_u + \beta \mathbf{K}_u$  (cf. [12]). The coefficients  $\alpha$  and  $\beta$  are related to the loss factor  $\tan \delta_i$  via the equation  $\tan \delta_i = (\alpha + \beta \omega_i^2) / \omega_i$  with  $\omega_i$  being the  $i$ -th eigenfrequency of the mechanical systems. For the computation of the coefficients from measured data we refer to [13]. The right hand side vector  $\underline{f}_e$  is due to the scalar electric potential given by the Dirichlet boundary conditions. The components of the coupling stiffness matrix  $\mathbf{K}_{uV}$  compute element-wise as (for the other matrices see, e.g., [13])

$$\mathbf{K}_{uV} = \bigwedge_{e=1}^{n_e} \mathbf{k}_{uV}^e; \quad \mathbf{k}_{uV}^e = [\mathbf{k}_{pq}]; \quad \mathbf{k}_{pq} = \int_{\Omega_e} \mathcal{B}_p^t [e]^t \tilde{\mathcal{B}}_q \, d\Omega$$

with  $n_e$  being the number of finite elements and  $\Omega_e$  the domain of one element. For time discretization we apply an implicit Newmark scheme with integration parameters  $\beta_H = 0.25$  and  $\gamma_H = 0.5$  to achieve an A-stable, 2nd order scheme [12]. For computations in the frequency domain we perform a Fourier transformation resulting in

$$\begin{pmatrix} \mathbf{K}_u + j\omega \mathbf{C}_u - \omega^2 \mathbf{M}_u & \mathbf{K}_{uV} \\ \mathbf{K}_{uV}^t & \mathbf{K}_{VV} \end{pmatrix} \begin{pmatrix} \hat{\mathbf{u}} \\ \hat{\underline{V}} \end{pmatrix} = \begin{pmatrix} 0 \\ \hat{\underline{f}}_e \end{pmatrix}$$

for the complex valued quantities  $\hat{\mathbf{u}}$  and  $\hat{\underline{V}}$ .

## 2.2 Mechanical coupling for nonmatching grids

Without loss of generality, we consider two sub-domains  $\Omega_1$  and  $\Omega_2$  (as can be seen in Fig. 2) on which we just consider the mechanical field. Therewith, the variational form of the mechanical PDE (2.3) after applying Green's integral theorem for two subdomains

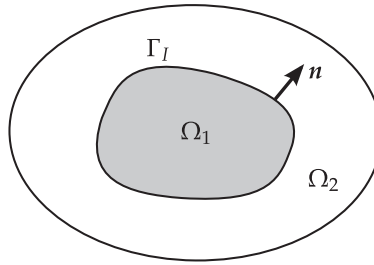


Figure 2: Subdomains for mechanical coupling.

reads as follows: Find  $\mathbf{u}_{1,2} \in \mathcal{V}_0$  such that

$$\int_{\Omega} \rho_1 \mathbf{u}'_1 \cdot \ddot{\mathbf{u}}_1 \, d\Omega + \int_{\Omega} (\mathcal{B}\mathbf{u}'_1)^t [c_1] \mathcal{B}\mathbf{u}_1 \, d\Omega - \int_{\Gamma} \mathbf{u}'_1 \cdot [\sigma_1] \mathbf{n} \, d\Gamma = \int_{\Omega} \mathbf{u}'_1 \cdot \mathbf{f}_{\Omega} \, d\Omega,$$

$$\int_{\Omega} \rho_2 \mathbf{u}'_2 \cdot \ddot{\mathbf{u}}_2 \, d\Omega + \int_{\Omega} (\mathcal{B}\mathbf{u}'_2)^t [c_2] \mathcal{B}\mathbf{u}_2 \, d\Omega + \int_{\Gamma} \mathbf{u}'_2 \cdot [\sigma_2] \mathbf{n} \, d\Gamma = 0$$

is fulfilled for all  $\mathbf{u}'_{1,2} \in \mathcal{V}_0$ . Here  $\rho_{1,2}$ ,  $[c]_{1,2}$ ,  $\sigma_{1,2}$  denote the mechanical densities, tensors of stiffness coefficients and stress tensors on the sub-domains. Sub-domain  $\Omega_1$  may be identified as piezoelectric patch since there acts the volumetric force  $\mathbf{f}_{\Omega}$  while sub-domain  $\Omega_2$  may be identified with the membrane/plate structure.

Both sub-domains share an internal surface  $\Gamma_I$ . On this surface we impose a weak condition on the mechanical displacement [12]

$$\int_{\Gamma_I} (\mathbf{u}_1 - \mathbf{u}_2) \boldsymbol{\mu} \, d\Gamma = 0, \tag{2.12}$$

with  $\boldsymbol{\mu}$  from a suitable Lagrange multiplier space  $M^{nd}$  (cf. [3, 8, 16]). Furthermore, we apply a strong condition on the normal stresses by introducing the Lagrange multiplier (LM)  $\lambda$

$$\lambda = -[\sigma_1] \cdot \mathbf{n} = -[\sigma_2] \cdot \mathbf{n}. \tag{2.13}$$

Therefore, the coupled problem reads as follows

$$\sum_{i=1}^2 \left( \int_{\Omega_i} \rho_i \mathbf{u}'_i \cdot \ddot{\mathbf{u}}_i \, d\Omega + \int_{\Omega_i} (\mathcal{B}\mathbf{u}'_i)^t [c_i] \mathcal{B}\mathbf{u}_i \, d\Omega \right) - \int_{\Omega_1} \mathbf{u}'_1 \cdot \mathbf{f}_{\Omega} \, d\Omega + \int_{\Gamma_I} (\mathbf{u}'_2 - \mathbf{u}'_1) \lambda \, d\Gamma = 0, \tag{2.14a}$$

$$\int_{\Gamma_I} (\mathbf{u}_1 - \mathbf{u}_2) \boldsymbol{\mu} \, d\Gamma = 0. \tag{2.14b}$$

Without loss of generality we identify  $\Omega_1$  as slave or non-mortar side and choose the trace of the finite element basis functions defined on this subdomain as a basis for the

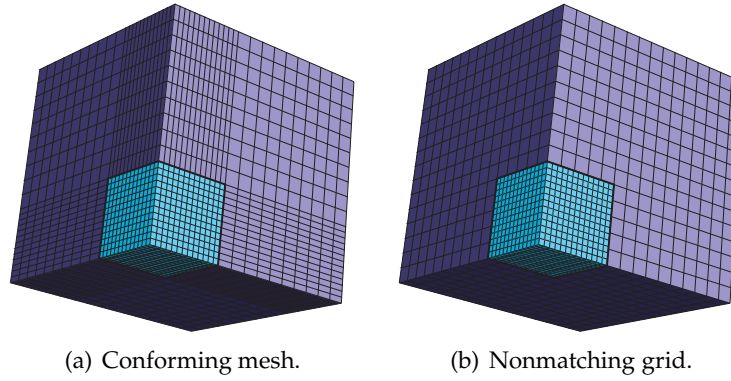


Figure 3: Conforming mesh vs. nonmatching grid in 3D.

Lagrange multiplier  $\lambda$  (and also  $\mu$ ). This choice is referred to as standard LM in the literature (cf. [3, 9]). Since the meshes in the two subdomains do not match in general, the integrals over the interface involving the traces of the functions on  $\Omega_2$  and the LM have to be evaluated with respect to different meshes as can be clearly seen in Fig. 3. This makes the introduction of intersection operators necessary which determine the lines or areas of intersection of the element faces on the interface. The integrals are then evaluated in respect to these intersection lines or areas (cf. [8]). After discretizing Eq. (2.14) using standard Lagrange (nodal) finite elements one arrives at the following semi-discrete system of equations

$$\begin{pmatrix} \mathbf{M}_{u1} & 0 & 0 \\ 0 & \mathbf{M}_{u2} & 0 \\ 0 & 0 & 0 \end{pmatrix} \begin{pmatrix} \ddot{\mathbf{u}}_1 \\ \ddot{\mathbf{u}}_2 \\ \ddot{\lambda} \end{pmatrix} + \begin{pmatrix} -\mathbf{K}_{u1} & 0 & \mathbf{D}^t \\ 0 & \mathbf{K}_{u2} & \mathbf{M}^t \\ \mathbf{D} & \mathbf{M} & 0 \end{pmatrix} \begin{pmatrix} \mathbf{u}_1 \\ \mathbf{u}_2 \\ \lambda \end{pmatrix} = \begin{pmatrix} \mathbf{f}_\Omega \\ 0 \\ 0 \end{pmatrix}.$$

The new matrices  $\mathbf{D}$  and  $\mathbf{M}$  are due to the nonconforming interface and are formally mass matrices, and compute element-wise as follows

$$\mathbf{D} = \bigwedge_{e=1}^{n_{es}} \mathbf{d}^e; \quad \mathbf{d}^e = [\mathbf{d}_{ab}]; \quad \mathbf{d}_{ab} = \int_{\Gamma_e} \begin{pmatrix} N_a^j & 0 & 0 \\ 0 & N_a^j & 0 \\ 0 & 0 & N_a^j \end{pmatrix} \begin{pmatrix} \Phi_b^j & 0 & 0 \\ 0 & \Phi_b^j & 0 \\ 0 & 0 & \Phi_b^j \end{pmatrix} d\Gamma, \quad (2.15)$$

$$\mathbf{M} = \bigwedge_{e=1}^{n_{isec}} \mathbf{m}^e; \quad \mathbf{m}^e = [\mathbf{m}_{ab}]; \quad \mathbf{m}_{ab} = \int_{\Gamma_e} \begin{pmatrix} N_a^k & 0 & 0 \\ 0 & N_a^k & 0 \\ 0 & 0 & N_a^k \end{pmatrix} \begin{pmatrix} \Phi_b^j & 0 & 0 \\ 0 & \Phi_b^j & 0 \\ 0 & 0 & \Phi_b^j \end{pmatrix} d\Gamma. \quad (2.16)$$

Here  $n_{es}$  is the number of surface elements on the slave side of the interface and  $n_{isec}$  is the number of intersection elements on the interface. The finite element basis functions  $N_a^j$  and  $N_a^k$  denote the traces of the FE basis on the slave and on the master side of the interface and  $\Phi_b^j$  denotes the Lagrange Multiplier basis given with respect to the slave side. For a detailed discussion on the intersection operators we refer to [8, 10].

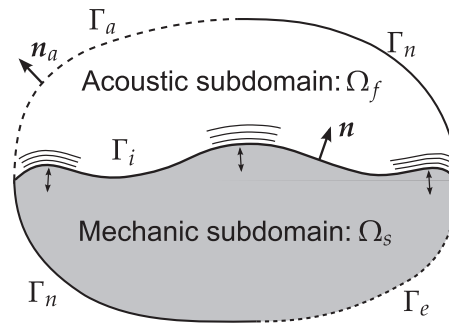


Figure 4: Subdomains for mechanic acoustic coupling.

### 2.3 Mechanical-acoustic coupling for nonmatching grids

Since we wish to simulate the sound radiation of a vibrating metal plate, which gets excited by attached piezoelectric actuators, we introduce here the equations for coupling the displacement based mechanical PDE with the pressure based linear acoustic wave equation. For the derivation of the coupling we consider two subdomains  $\Omega_s$  and  $\Omega_f$  for mechanics and acoustics. In subdomain  $\Omega_s$  the equation of linear elasticity (see (2.3)) and in  $\Omega_f$  the acoustic wave equation

$$\Delta p' = \frac{1}{c^2} \frac{\partial^2 p'}{\partial t^2} \tag{2.17}$$

have to be solved. In (2.17)  $p'$  denotes the acoustic pressure and  $c$  the speed of sound. The boundaries  $\Gamma_n$ ,  $\Gamma_e$  and  $\Gamma_a$  in Fig. 4 refer to the general case of the boundary divided into subsets with Neumann, Dirichlet and absorbing boundary conditions.

To enforce the coupling between the two subdomains, we require the continuity of the normal mechanical and acoustic particle velocities over the interface  $\Gamma_i$ . In terms of the alternating acoustic pressure and the mechanical displacement this condition may be written in the following way [13]

$$-\frac{1}{\rho_f} \mathbf{n} \cdot \nabla p' = \mathbf{n} \cdot \frac{\partial^2 \mathbf{u}}{\partial t^2}. \tag{2.18}$$

Here  $\rho_f$  denotes the density of the acoustic fluid. The second coupling condition states that the total pressure load from the ambient fluid to the mechanical body is equal to its mechanical stress in normal direction,

$$[\sigma] \cdot \mathbf{n} = -\mathbf{n} p'. \tag{2.19}$$

By inserting condition (2.18) into the surface integral of the weak form of the acoustic

wave equation<sup>‡</sup>

$$\int_{\Omega} \frac{1}{c^2} w \ddot{p}' \, d\Omega + \int_{\Omega} \nabla w \cdot \nabla p' \, d\Omega + \int_{\Gamma} w \mathbf{n} \cdot \nabla p' \, d\Gamma = 0, \quad (2.20)$$

we arrive at

$$\int_{\Omega} \frac{1}{c^2} w \ddot{p}' \, d\Omega + \int_{\Omega} \nabla w \cdot \nabla p' \, d\Omega - \int_{\Gamma} \rho_f w \mathbf{n} \cdot \dot{\mathbf{u}} \, d\Gamma = 0. \quad (2.21)$$

Condition (2.19) is used to replace the surface integral term arising in the weak form of (2.3). This results in

$$\int_{\Omega} \rho_s \mathbf{u}' \cdot \dot{\mathbf{u}} \, d\Omega + \int_{\Omega} (\mathcal{B} \mathbf{u}')^t [c] \mathcal{B} \mathbf{u} \, d\Omega + \int_{\Gamma_i} \mathbf{u}' \cdot n p' \, d\Gamma = \int_{\Omega} \mathbf{u}' \cdot \mathbf{f}_{\Omega} \, d\Omega, \quad (2.22)$$

where  $\mathbf{u}'$  is the finite element test function,  $\rho_s$  denotes the density of the solid material and  $\mathbf{f}_{\Omega}$  is a volume force applied to the body. After discretizing the above equations using standard Lagrange finite elements one arrives at the un-symmetric, semi-discrete system of equations

$$\begin{pmatrix} \mathbf{M}_p & \mathbf{M}_{pu} \\ 0 & \mathbf{M}_u \end{pmatrix} \begin{pmatrix} \ddot{\underline{p}} \\ \ddot{\underline{u}} \end{pmatrix} + \begin{pmatrix} \mathbf{K}_p & 0 \\ \mathbf{K}_{up} & \mathbf{K}_u \end{pmatrix} \begin{pmatrix} \underline{p} \\ \underline{u} \end{pmatrix} = \begin{pmatrix} 0 \\ \underline{f}_u \end{pmatrix}.$$

The new coupling matrices  $\mathbf{M}_{pu}$  and  $\mathbf{K}_{up}$  are calculated as follows

$$\mathbf{M}_{pu} = \rho_f \mathbf{K}_{up}^T, \quad (2.23)$$

$$\mathbf{K}_{up} = \bigwedge_{e=1}^{n_{\text{isec}}} \mathbf{k}^e; \quad \mathbf{k}^e = [\mathbf{k}_{ab}]; \quad \mathbf{k}_{ab} = \int_{\Gamma_e} \begin{pmatrix} N_a^j N_b^k n_x \\ N_a^j N_b^k n_y \\ N_a^j N_b^k n_z \end{pmatrix} d\Gamma. \quad (2.24)$$

Here  $\bigwedge$  is the element-wise FE assembly operator and  $n_{\text{isec}}$  is the number of intersection elements on the interface since the surface integrals over  $\Gamma_i$  have to be evaluated with respect to different grids (cf. Fig. 3). The time discretization is again performed by an implicit Newmark method for both the mechanical and acoustic quantities with  $\beta_H = 0.25$  and  $\gamma_H = 0.5$  to achieve at an A-stable scheme. For frequency computation we apply a Fourier transformation as described in Section 2.1.

<sup>‡</sup>Note: The surface integral in Eq. (2.20) has a positive sign, because the normal vector of the acoustic domain  $\Omega_f$  is opposite to  $\mathbf{n}$  (see Fig. 4).

### 3 Numerical example: Excitation and active damping of a metal plate using piezoelectric patches

#### 3.1 Problem description

In order to show the great flexibility of the Mortar FEM we examine a setup of a metal plate which radiates acoustic waves into an air volume due to an excitation by attached piezoelectric actuators. We conduct harmonic simulations to examine the response of the system to different excitation frequencies.

We present a standard FE model of this setup to demonstrate the drawbacks which our method is able to overcome. The main drawback is indeed the need for a geometrically conforming mesh in all subdomains. This requirement is of purely mathematical nature and prohibits us to take advantage of the physical requirements in different subdomains. To strengthen this point we consider the acoustic wave length in air at 100 Hz, which is  $\lambda = 3.4\text{m}$ . This would permit the usage of linear finite elements with an edge length of about  $\lambda/20 = 17\text{cm}$ . The metal plate which excites the acoustic wave is however of rectangular dimensions 50 cm by 30 cm by 1 mm. Therewith, we discretize the plate as a 3D solid and use 2nd order finite element basis functions with a special selected reduced integration technique to totally avoid locking [7]. To accurately simulate the mechanical deformations of this plate we need to apply a mesh size of about 5 mm in the plane and 1 mm in thickness direction. This means that the acoustic mesh size may be one order of magnitude (34 times at 100 Hz) larger in plane direction than the mesh size for the mechanical computation.

The standard FEM restricts us however to either use structured meshes, which carry on the fine discretization of mechanics all the way into the acoustic subdomain. This gives rise to an unnecessary high number of unknowns. Or we could use an unstructured mesh which admits the coarsening of elements at the cost of an increasing numerical error due to distorted element shapes.

By allowing nonmatching grids on different subdomains the Mortar FEM does not only give us a free hand in choosing the right discretization for different physical fields but also enhances our flexibility to freely place the piezoelectric patches on the metal plate. In contrast, the standard FEM would require the remeshing of the whole computational domain for changing the positions of the patches. Another positive aspect of the Mortar FEM is, that the order of approximation may be chosen independently in each subdomain. We make use of this fact, by choosing quadratic Lagrangian hexahedral elements in our acoustic propagation domain.

The geometry for our setup consists of a metal plate of thickness 1 mm with two attached piezoelectric patches as depicted in Fig. 5. The thickness of both patches is also 1 mm. They are attached below the plate in the given positions. The top surface of the plate coincides with  $z = 0$ . The bottom surface of the acoustic domain also coincides with the plane  $z = 0$ . The acoustic propagation domain extends 80 cm in  $z$ -direction. An additional 20 cm layer for applying a perfectly matched layer (cf. [5]) to simulate

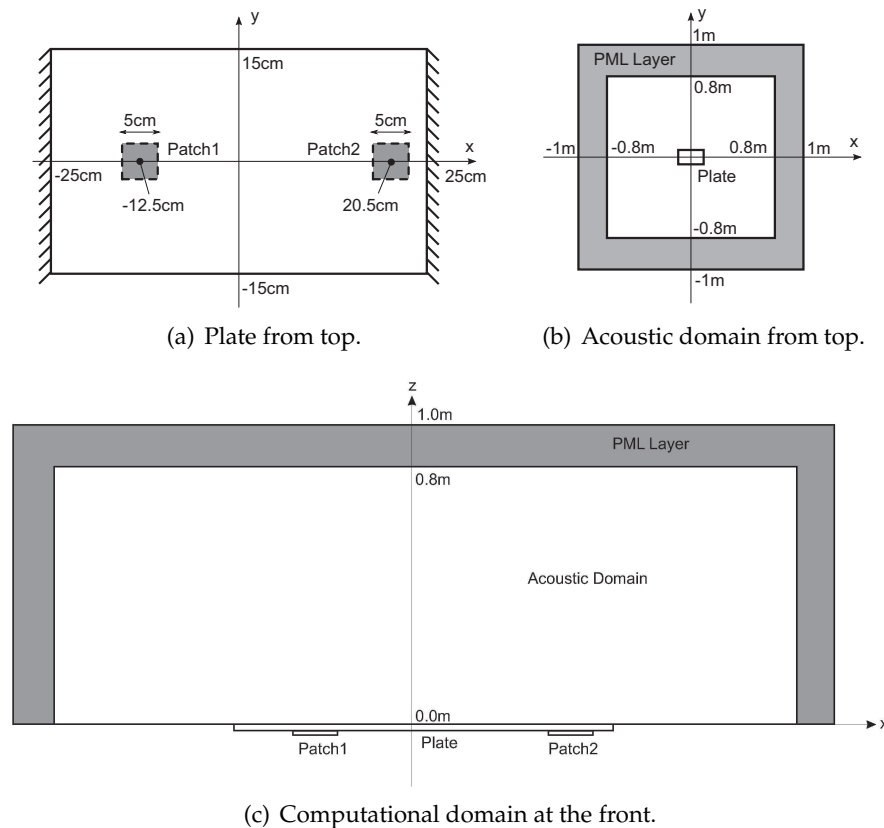


Figure 5: Setup of computational domain (for display reasons not at scale).

free field radiation is added on top of the propagation domain. As materials we choose aluminum for the plate, lead zirconate titanate (PZT-4) for both patches and air for the acoustic propagation region. For the electrostatic field we apply homogeneous Dirichlet conditions on the bottom electrodes and inhomogeneous Dirichlet conditions on the top electrodes to prescribe the electric potential. Homogenous Neumann conditions are used on the rest of the faces. The plate is mechanically fixed for all degrees of freedom on its left and right boundaries and may move freely anywhere else.

### 3.2 Problem formulation

According to our formulations described in Section 2.1 (piezoelectricity), Section 2.2 (mechanical-mechanical coupling) and Section 2.3 (mechanical-acoustic coupling) we can now apply the Mortar-FEM to our setup. Therewith, we allow a non-matching interface between the piezoelectric patches and the bottom surface of the plate as well as the top surface of the plate and the ambient acoustic computational domain. Since our application considers the computation in the frequency domain, we arrive at the following

complex algebraic system of equations

$$\begin{pmatrix} \mathbf{K}_{u_1}^* & 0 & \mathbf{D}^t & \mathbf{K}_{u_1V} & 0 \\ 0 & \mathbf{K}_{u_2}^* & \mathbf{M}^t & 0 & \mathbf{K}_{u_2p} \\ \mathbf{D} & \mathbf{M} & 0 & 0 & 0 \\ \mathbf{K}_{u_1V}^t & 0 & 0 & -\mathbf{K}_{VV} & 0 \\ 0 & -\omega^2 \mathbf{M}_{pu_2} & 0 & 0 & \mathbf{K}_p^* \end{pmatrix} \begin{pmatrix} \hat{u}_1 \\ \hat{u}_2 \\ \hat{\lambda} \\ \hat{V} \\ \hat{p} \end{pmatrix} = \begin{pmatrix} 0 \\ 0 \\ 0 \\ \hat{f}_e \\ 0 \end{pmatrix}$$

with  $\mathbf{K}_{u_1}^* = -\mathbf{K}_{u_1} + j\omega \mathbf{C}_{u_1} - \omega^2 \mathbf{M}_{u_1}$ ,  $\mathbf{K}_{u_2}^* = \mathbf{K}_{u_2} + j\omega \mathbf{C}_{u_2} - \omega^2 \mathbf{M}_{u_2}$  and  $\mathbf{K}_p^* = \mathbf{K}_p - \omega^2 \mathbf{M}_p$ .

### 3.3 Numerical results

**Comparison Between Conforming and Mortar FEM Model** In order to compare the results for the conforming FEM model to the results computed with the Mortar FEM we just apply a voltage load to Patch1 and compare the resulting mechanical displacement amplitude fields in  $z$ -direction and the acoustic pressure field on a plane 50 cm above the plate. We conduct the simulations at a frequency of 80 Hz. In Fig. 6 the meshes in the vicinity of Patch2 for the standard model and the Mortar FEM model can be seen. Both meshes consist of 20-node serendipity hexahedral elements. The mesh for the plate and the patches (edge length  $h=5$  mm in  $x$ - $y$ -plane) is reused in the Mortar model. Therefore these meshes are geometrically conforming even in the nonmatching case. The interface between them is however treated as a mechanical nonmatching interface. The mesh for the air volume is replaced by a uniform grid with an edge length  $h=4$  cm. With this setup it should be possible to resolve the acoustic wave field up to a frequency of 1 kHz. The wave length for this frequency is  $\lambda = 34$  cm and we therefore resolve it with about  $34\text{cm}/2\text{cm} = 17$  degrees of freedom. Some elements in the air volume of the conforming grid have a very bad aspect ratio due to the requirement of geometrical conformity (i.e. no hanging nodes are allowed). Due to this requirement a comparison of the results of the two methods for higher frequencies than 100 Hz is quite unfair. This may be attributed to the fact that too many degrees of freedom are wasted by having to continue the fine plate discretization into the air volume. With a given amount of system memory one has no degrees of freedom left for refining the other parts of the acoustic domain and is therefore restricted to low frequencies.

Fig. 7 shows the amplitude fields of the  $z$ -component of the mechanical displacement at 80 Hz. A good agreement between the standard FEM and the Mortar FEM model may be observed. The sound pressure amplitude field at a height of 50 cm above the plate is depicted in Fig. 8. The field on the conforming grid clearly suffers from the difference in element sizes which can be deduced from the isolines. The isolines are smooth for the nonmatching grid. This means, that the simulation on a nonmatching grid yields even better results as the standard method. Since we are able to independently discretize the

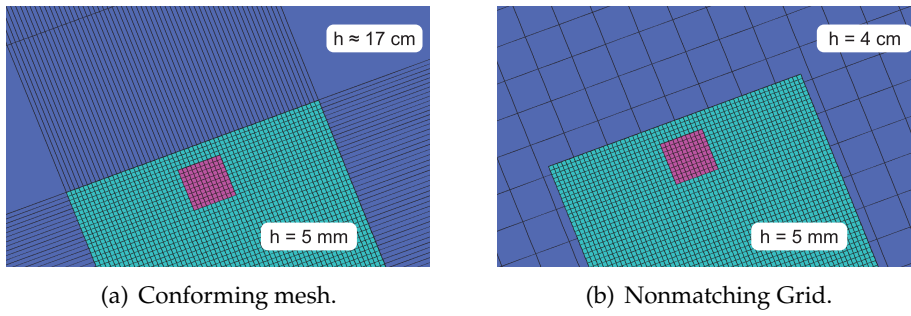


Figure 6: Meshes in the vicinity of Patch2.

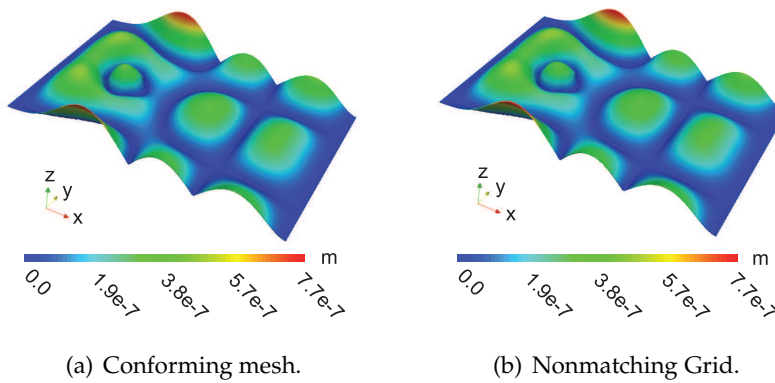


Figure 7: Amplitude of z-component of the mechanical displacement at  $z = 50 \text{ cm}$  (at  $80 \text{ Hz}$ ).

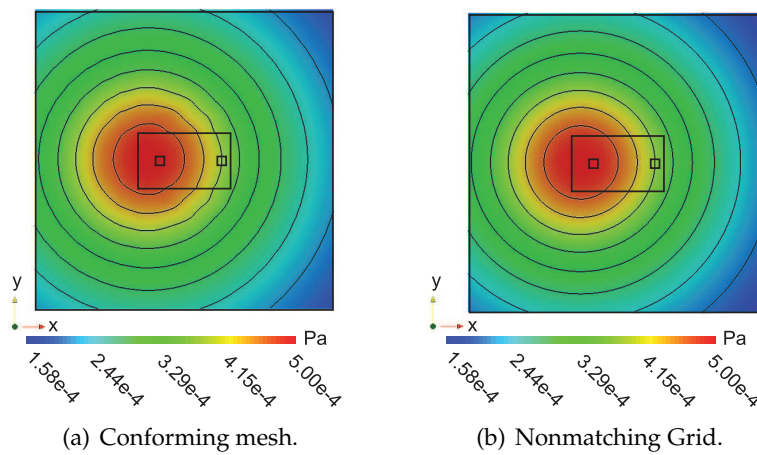


Figure 8: Amplitude of sound pressure at  $z = 50 \text{ cm}$  (at  $80 \text{ Hz}$ ).

mechanical parts and the acoustic domain, we can adjust the acoustic mesh size to allow much higher frequencies than would be possible using the standard FEM.

Table 1: Number of (complex-valued) unknowns and wall clock times.

Physical Field	Conforming Mesh	Nonmatching Grid
Electric Potential	1,265	1,265
Mechanical Displacement	121,713	123,759
Acoustic Pressure	205,709	265,251
Lagrange Multiplier	-	2,046
<b>Total</b>	<b>328,687</b>	<b>392,321</b>
<b>Wall Clock Times (s)</b>	<b>154</b>	<b>250</b>

In Table 1 we present the number of unknowns for both meshes. We note that while having only 19.4% additional unknowns the nonmatching grid can handle frequencies of up to 1 kHz whereas the conforming mesh supports only frequencies of up to 100 Hz due to large elements in the corners of the acoustic domain. Trying to refine these elements comes at the cost of having to introduce a large number of additional elements in the neighborhood of the plate, due to its fine discretization. The last row in Table 1 shows the computational wall clock times needed for the simulations. The corresponding simulation runs are performed on a 16-core AMD Opteron 8380 shared memory machine. Only twelve cores are used and the arising linear complex algebraic system of equations is solved using the sparse direct solver PARDISO [14].

**Higher Frequencies** As mentioned in the previous section a lot of unknowns are wasted by having to continue the fine discretization of the plate into the acoustic region. For our first comparison at 80 Hz no mentionable effects of this shortcoming can be observed. The situation changes however if the comparison is repeated for higher frequencies. Fig. 9(a) shows the sound field and the displacement field of the plate at 250 Hz. Even though the wave length  $\lambda = 1.36\text{m}$  is still resolved by about 16 degrees of freedom in the coarse regions of the acoustic domain, the computed sound field is completely screwed up in comparison with the nonmatching grid in Fig. 9(b). The situation gets even worse as we further increase the frequency. At 1 kHz the conforming grid would just resolve a wave with 4 degrees of freedom in the coarse parts. This is in no way a suitable discretization any more. Therefore just the result for the nonmatching grid is shown in Fig. 9(c). One can obviously see that the sound field is very smooth. This comparison shows the advantages of using nonmatching grids in a striking way. Using around the same number of unknowns the nonmatching grid can predict sound fields with a frequency ten times as large as would be possible with the conforming grid for our configuration.

**Compensation using Negative Voltage Loading on Patch 2** In order to actively compensate the displacements generated by Patch1, we apply the inverse voltage (-10 V) to Patch2. This indeed reduces the amplitudes of the plate's vibration as expected (see Fig. 10). Indeed, for the investigated setup, the position of Patch2 is already the optimal one. Changing its position just by some small amount, as shown in Fig. 10, strongly increases

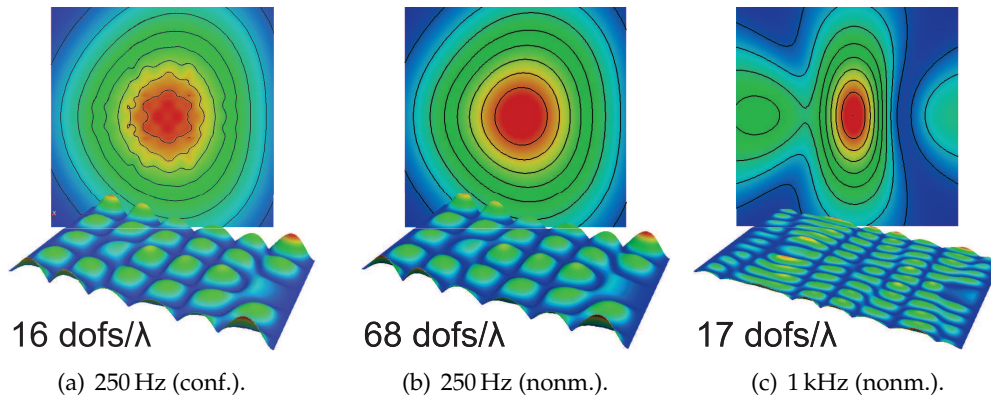


Figure 9: Mechanical displacement of the plate and acoustic pressure 50 cm above the plate for conforming and nonmatching setup at 250 Hz and for the nonmatching setup at 1 kHz.

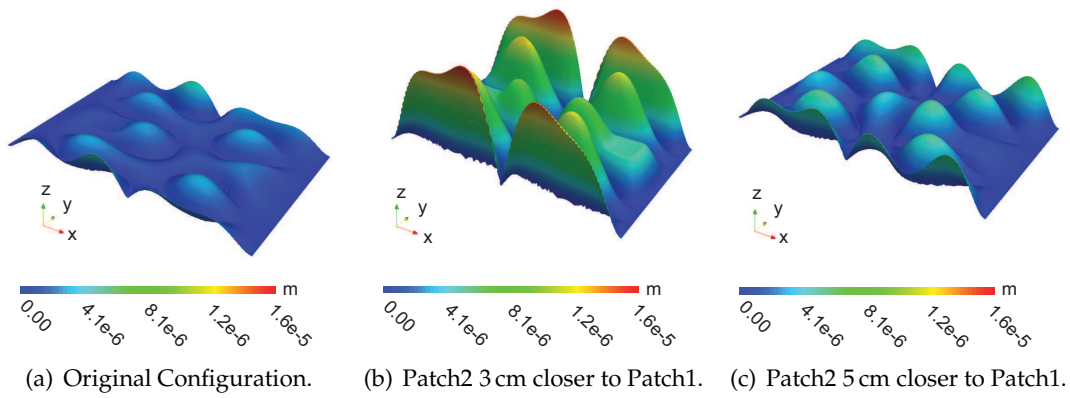


Figure 10: Mechanical displacements on plate for different positions of Patch2.

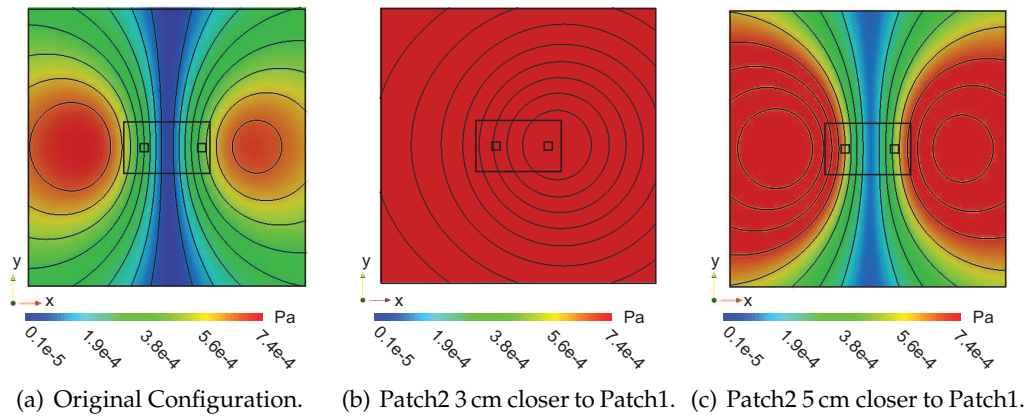


Figure 11: Acoustic amplitude field at  $z=50$  cm for different positions of Patch2.

the mechanical vibration amplitude and furthermore the radiated sound as demonstrated in Fig. 11.

## 4 Conclusion and outlook

We have shown that the Mortar FEM is well-suited for the computation of slender vibrating mechanical structures excited by piezoelectric patches. We get better results in comparison to the standard FEM and obtain a higher degree of flexibility for modeling the computational domain at the same time. Given the same number of unknowns, the range of frequencies the Mortar FEM mesh can handle is much broader than in the conforming case. Finally, we want to mention, that our method is used as a building block for optimization schemes which can find the optimal position of the piezoelectric actuators on plate/membrane structures (cf. [15]).

## Acknowledgments

This work was supported by the German Research Foundation (DFG) under grant WO 671/6-2 and the Austrian Science Foundation (FWF) under grant I 533-N20. We would like to thank the DFG and the FWF for their support.

## References

- [1] R. Adams. Sobolev Spaces. Pure and Applied Mathematics, Academic Press, 1975.
- [2] A. Bamberger, R. Glowinski, and Q. H. Tran. A domain decomposition method for the acoustic wave equation with discontinuous coefficients and grid change. *SIAM J. Numer. Anal.*, 34(2):603–639, 1997.
- [3] F. B. Belgacem. The mortar finite element method with lagrange multipliers. *Numer. Math.*, 84(2):173–197, 1999.
- [4] F. B. Belgacem. A stabilized domain decomposition method with nonmatching grids for stokes problem in three dimensions. *SIAM J. Numer. Anal.*, 42(2):667–685, 2004.
- [5] J.-P. Berenger. A perfectly matched layer for the absorption of electromagnetic waves. *J. Comput. Phys.*, 114(2):185–200, 1994.
- [6] C. Bernardi, Y. Maday, and A. T. Patera. A new nonconforming approach to domain decomposition: The mortar element method. In *Nonlinear partial differential equations and their applications. Collège de France Seminar, Vol. XI (Paris, 1989–1991)*, volume 299 of Pitman Res. Notes Math. Ser., pages 13–51. Longman Sci. Tech., Harlow, 1994.
- [7] D. Braess and M. Kaltenbacher. Efficient 3d-finite-element-formulation for thin mechanical and piezoelectric structures. *Int. J. Numer. Meth. Engr.*, 73(2):147–161, 2008.
- [8] B. Flemisch. Non-matching Triangulations of Curvilinear Interfaces Applied to Electro-Mechanics and Elasto-Acoustics. PhD thesis, University of Stuttgart, Institute for Applied Analysis and Numerical Simulation, 2006.
- [9] B. Flemisch, M. Kaltenbacher, and B. Wohlmuth. Elasto-acoustic and acoustic-acoustic coupling on nonmatching grids. *Int. J. Numer. Meth. Engr.*, 67(13):1791 – 1810, 2005.

- [10] M. J. Gander and C. Japhet. An algorithm for non-matching grid projections with linear complexity. In *Domain Decomposition Methods in Science and Engineering XVIII*, volume 70, pages 185–192. Springer, 2009.
- [11] B. Ganis and I. Yotov. Implementation of a mortar mixed finite element method using a Multiscale Flux Basis. *Comput. Meth. Appl. Mech. Engr.*, 198:3989–3998, 2009.
- [12] T. J. Hughes. *The Finite Element Method*. Dover, Mineola, N.Y., 1. edition, 2000.
- [13] M. Kaltenbacher. *Numerical Simulation of Mechatronic Sensors and Actuators*. Springer, Berlin, 2. edition, 2007.
- [14] O. Schenk and K. Gärtner. Solving unsymmetric sparse systems of linear equations with pardiso. *Future Gener. Comput. Syst.*, 20(3):475–487, 2004.
- [15] F. Wein, M. Kaltenbacher, E. Bänsch, G. Leugering, and F. Schury. Topology optimization of a piezoelectric-mechanical actuator with single- and multiple-frequency excitation. *Int. J. App. Electromag. Mech.*, 30:201–221, 2009.
- [16] B. Wohlmuth. A mortar finite element method using dual spaces for the Lagrange multiplier. *SIAM J. Numer. Anal.*, 38(3):989–1012, 2000.
- [17] B. I. Wohlmuth. A comparison of dual Lagrange multiplier spaces for mortar finite element discretizations. *M2AN Math. Model. Numer. Anal.*, 36(6):995–1012, 2002.